RSC Advances

PAPER

View Article Online
View Journal | View Issue



Cite this: *RSC Adv.*, 2025, **15**, 47282

# A computational insight of the physical properties of MoSX (X= Cl, Br, I) for green energy applications

Muhammad Yousuf,[a] Ali Raza,[a] Farooq Ali,[a] Hamid Ullah, *[a] Young-Han Shin [b] and Essam A. Al-Ammar[c]

Received 25th September 2025
Accepted 25th November 2025

DOI: 10.1039/d5ra07274c

rsc.li/rsc-advances

We employed first-principles DFT calculations to investigate the structural, optoelectronic, and thermoelectric properties of halide-based MoSX (X = Cl, Br, I) materials. We observed that these materials exhibit an energetically stable nature due to lower formation energies. MoSX (X = Cl, Br, I) possess a semiconducting behavior with bandgaps ranging from 1.24 eV to 1.38 eV. Notably, MoSCl and MoSBr show a direct bandgap, which is advantageous for optoelectronic devices such as light-emitting diodes and solar cells. Moreover, the calculated figure of merit (*ZT*) values highlight the suitability of MoSX (X = Cl, Br, I) for thermoelectric applications. These findings establish a theoretical foundation for experimentalists to pursue applications in solar energy generation and thermal energy management.



## 1 Introduction

The global transition toward sustainable energy systems has intensified the search for advanced materials capable of driving innovations in green energy technologies, such as photocatalysis, photovoltaics, and energy storage.[1–4] The transition metal dichalcogenide (TMD) materials, renowned for their exceptional electronic, optical, and mechanical properties, have emerged as frontrunners in this quest.[1,5–7] Among these, the $MoS_2$ have garnered significant attention due to their tunable bandgaps and high carrier mobility.[1,8] However, the intrinsic symmetry of conventional TMDs limits their functionality in applications requiring built-in polarization or asymmetric charge distribution.[9,10]

This limitation has spurred interest in this new class of materials[2,7,11,12] with exceptional properties, such as broken mirror symmetry, inducing a vertical dipole moment and piezoelectricity, which enhance charge separation and interfacial reactivity.[13] Recent advances in synthesis, including the pioneering work by Lu *et al.*[13] on MoSSe *via* selective epitaxy, have demonstrated the feasibility of creating such asymmetric architectures.[11,14–16] Computational studies further predict that tailoring the Janus composition can modulate electronic and optical properties, making them ideal for energy conversion.[2,12,16,17]

Halide-based Janus materials, particularly MoSX (X = Cl, Br, I), represent an underexplored frontier. Replacing one chalcogen layer with a halogen atom introduces significant electronegativity contrast, potentially amplifying built-in electric fields and enabling novel bandgap engineering.[2,13,18] For instance, Waheed *et al.*,[3] Asghar *et al.*,[16] and manymore[7,11,12,17] computationally demonstrated that MoSX exhibits enhanced structural stability and anisotropic carrier mobility compared to symmetric TMDs.[13] The tunability of halides (Cl, Br, I) also allows systematic control over electronic properties: lighter halides like Cl widen bandgaps, while heavier counterparts (I) reduce them, aligning with requirements for visible-light photocatalysis.[19–22] Moreover, the intrinsic polarization in Janus MoSX promotes efficient electron–hole separation, a critical factor for hydrogen evolution reactions (HER) and solar fuel generation.[10,18,23]

Despite these prospects, comprehensive computational insights into the physicochemical properties of MoSX systems remain sparse. Previous studies have focused on chalcogen-based Janus materials, leaving halide variants relatively unexplored. This knowledge gap hinders the rational design of MoSX for targeted applications. For example, the role of halogen electronegativity in modulating interfacial charge transfer—key for photocatalytic water splitting—requires deeper scrutiny.[3,11,19]

In this study, we employ density functional theory (DFT) simulations to unravel the structural stability, electronic structure, optical absorption, and thermoelectric properties of MoSX (X = Cl, Br, I). By analyzing the interplay between halogen choice and material properties, we aim to establish design principles for optimizing these materials in green energy applications. Our findings reveal that MoSX exhibits a bandgap ranging 1.24–1.38 eV, strong absorption, and suitable *ZT* (~0.75) make them ideal for solar cells and thermoelectric applications. Ultimately, this computational framework provides a roadmap for synthesizing and integrating MoSX into next-generation energy technologies.

[a]*Department of Physics, RIPHAH International University, Lahore Campus, Pakistan. E-mail: hamid.uou@gmail.com*

[b]*Multiscale Materials Modeling Laboratory, Department of Physics, University of Ulsan, Ulsan 44610, Republic of Korea*

[c]*Department of Electrical Engineering, College of Engineering, King Saud University, P.O. Box 800, Riyadh 12372, Saudi Arabia*

## 2 Method and calculation

All calculations in this work were performed using first-principles density functional theory (DFT) as implemented in the WIEN2k package.[24] The exchange-correlation effects were treated using the Generalized Gradient Approximation (GGA) in the Perdew–Burke–Ernzerhof (PBE) parameterization.[25] The initial structural optimization was carried out by minimizing interatomic forces and stresses within the GGA framework to achieve equilibrium lattice parameters. The Birch–Murnaghan equation of state[26] was subsequently applied to fit the ground-state energy–volume curves.

In order to have reliable electronic properties, we used the Tran–Blaha modified Becke–Johnson (TB-mBJ) potential[27] to increase the accuracy. TB-mBJ is a well-established semi-local exchange-correlation functional capable of predicting bandgaps closer to experimental values than standard GGA.[27,28] The WIEN2k framework divides the crystal lattice into muffin-tin spheres which represent a harmonic expansion of the electron density, and an interstitial region which is described by plane waves. The basis set size was controlled by the parameter RMT $\times K_{max} = 8$, ensuring energy convergence. The Fourier expansion of the charge density and potential was truncated at $G_{max} = 16\ Ry^{-1}$, and the energy convergence was set to $1 \times 10^{-6}$ Ry. A k-mesh of $21 \times 21 \times 10$ was adopted for Brillouin zone integration, balancing the computational efficiency and precision. For the optical properties calculations, we followed the same techniques as in ref 2 and 29. For thermoelectric properties, including electrical conductivity and Seebeck coefficient, the semi-classical Boltzmann transport equations were solved under the constant relaxation time approximation using the BoltzTrap package.[30] This approach leverages the DFT-calculated band structure and carrier dispersion relations to evaluate transport coefficients as functions of temperature and chemical potential.

## 3 Result and discussion

### 3.1 Structural characteristics

The MoSX (X = Cl, Br, I) crystallizes in a cubic structure with the space group $F\bar{4}3m$ (# 216), which is confirmed by the Jain *et al.*.[31] The atomic positions within the unit cell are defined by the Wyckoff positions at 16e sites for Mo (0.35, 0.15, 0.85), S (0.12, 0.38, 0.62), and X (0.12, 0.38, 0.12), as illustrated in Fig. 1(a). Prior to computing the physical properties, structural optimization was performed to determine the ground state energies at different volumes, as illustrated in Fig. 1(b). From Fig. 1(b), one can observed that MoSBr possesses lower optimization energy in comparison to MoSCl and MoSI. The obtained lattice parameters for MoSX (X = Cl, Br, I) follows the trend and agreement with previously reported theoretical work.[2]

Our computed results indicate a monotonic increase in the lattice parameter (summarized in Table 1) from Cl to I, consistent with the increasing ionic radii of the halogens, following the relation $a_0 = V_0^{\frac{1}{3}}$. Conversely, the bulk modulus ($B_0$) exhibits a decreasing trend along the same series, adhering to the inverse proportionality $B_0 \propto \frac{1}{V_0}$.[29,32] Furthermore, one can see from Table 1, that bond length between Mo and S (denoted by $d_1$) remain unchanged, while it changes significantly between Mo and X (shown by $d_2$) atoms, which is due to difference in electronegativity.

The structural properties of these materials directly influence their electronic behavior. Variations in the lattice parameter, induced by anion substitution (Cl → Br → I)[29,32–34] or cation modification,[35,36] lead to tunable physical properties. Specifically, the increase in ionic radius from Cl to I results in lattice expansion and a concomitant reduction in the band gap. This trend arises from the decreased binding energy of valence electrons, which require less energy for excitation into the conduction band.

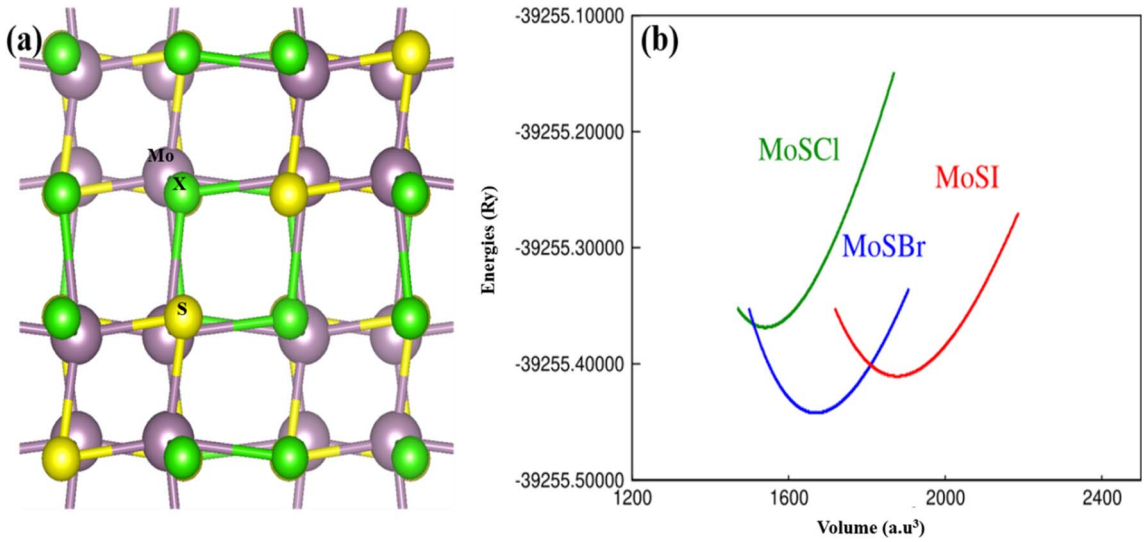


Fig. 1 The optimized (a) structure and (b) optimization curve of the bulk MoSX (X = Cl,Br,I). The Mo, S, and X (Cl, Br, I) are represent with color purple, yellow, and green.

Table 1 Calculated lattice constants, band gap, and distances between atoms of the MoSX

| Compound | $a_0$ (Å) | $d_1$ Mo-S(Å) | $d_2$ Mo-X(Å) | $E_f$ (eV) | $Eg$ (eV) |
|---|---|---|---|---|---|
| MoSCl | 9.70 | 2.32 | 2.62 | −1.28 | 1.38 |
| MoSBr | 9.96 | 2.32 | 2.76 | −0.97 | 1.31 |
| MoSI | 10.36 | 2.33 | 2.92 | −0.93 | 1.24 |

The thermodynamic stability of the investigated double perovskites is confirmed by the negative formation energies ($E_f = [E_{MoSX} - (E_{Mo} + E_S + E_X)]$, where $E_{MoSX}$, $E_{Mo}$, $E_S$, and $E_X$ representing the energies of the MoSX unit cell, the total energies of the Mo, S, and Cl atoms in their bulk form), as listed in Table 1. Notably, the magnitude of $E_f$ decreases progressively as the halide ion (X) varies from Cl to I.[29] This trend can be attributed to the increasing lattice constant, which enhances the effective interionic separation within the crystal lattice, thereby reducing the $E_f$. We have compared our results with the already available literature on bulk SnXY(X ≠ Y = S, Se)[2] and found a good agreement.

### 3.2. Electronic properties

The structural information-derived dataset was further subjected to energy convergence using the Tran–Blaha modified Becke–Johnson (TB-mBJ) potential. In general, the TB-mBJ potential yields computed band gaps that align well with experimental one.[37,38] Using the above assumptions, we calculate the bands for MoSX (X = Cl, Br, I) and the results are given in Fig. 2. The valence band maximum (VBM) and conduction band minimum (CBM) also lie at the *X*-point joint and a direct band gap of 1.38 eV, 1.31 eV is confirmed in MoSCl and MoSBr respectively. Both VBM and CBM of MoSI are situated at *Γ*- and *X*-points respectively, exhibiting a 1.24 eV indirect band gap character. MoSCl and MoSBr are shown to be direct band gap semiconductor which can be helpful for respective optoelectronic applications. The materials exhibiting a direct band gap facilitate efficient light absorption *via* electron transitions from the valence to the conduction band without requiring phonon mediation, enabling precise optical response at critical energies. As indicated in Table 1, the computed band gaps deviate from prior theoretical predictions SnSeX (X = S, O)[2] due to the mBJ potential's inherent state-shifting effects. While the mBJ potential is recognized for improving agreement with experimental band gaps, no experimental data exist for the studied MoSX (X = Cl, Br, I) compounds for direct validation.

For the photovoltaic efficiency, the ideal band gap range is 0.8–2.2 eV.[29,39] The computed band gaps of MoSX (X = Cl, Br, I) ranges from 1.24–1.38 eV fall within this range, The materials with band gap in this range exhibit properties comparable to lead-based perovskites while offering the advantage of non-toxicity, making them superior alternatives for photovoltaic applications.[40]

The electronic bands were further examined by computing the total/projected (T/PDOS). The TDOS and PDOS for MoSX (X = Cl, Br, I) were evaluated within an energy range of −4 eV to 4 eV, as illustrated in Fig. 3. The TDOS plots demonstrate that going from Cl to I induces a more pronounced downward shift in the conduction states compared to the upward displacement of the valence states. This asymmetric energy state displacement results in band gap narrowing and tunability.

The valence band maximum (VBM) is primarily formed by the hybridization of Mo-d and S-/X-p states, whereas the conduction band minimum (CBM) arises from the interaction between S-p and X-p states. This hybridization generates an effective attractive interaction, leading to a downward shift in the conduction band states (dominated by I Mo-d and S-/X-p). Consequently, the X (Cl, Br, I) atoms ionic radius critically governs the hybridization-driven band gap suppression, offering a practical pathway for tailoring optoelectronic materials with tunable spectral responses.

### 3.3 Effective masses and sound velocities

Additionally, we have calculated the effective masses and sound velocities of MoSX (X = C, Br, I). The calculated values of electronic ($m_e$) effective mass are 0.29 $m_0$, 0.23 $m_0$ and 0.19 $m_0$ for MoSCl, MoSBr and MoSI, respectively. However, for hole ($m_h$), the values of effective mass are found 0.75 $m_0$, 0.94 $m_0$ and 1.04 $m_0$ for MoSCl, MoSBr and MoSI, respectively.

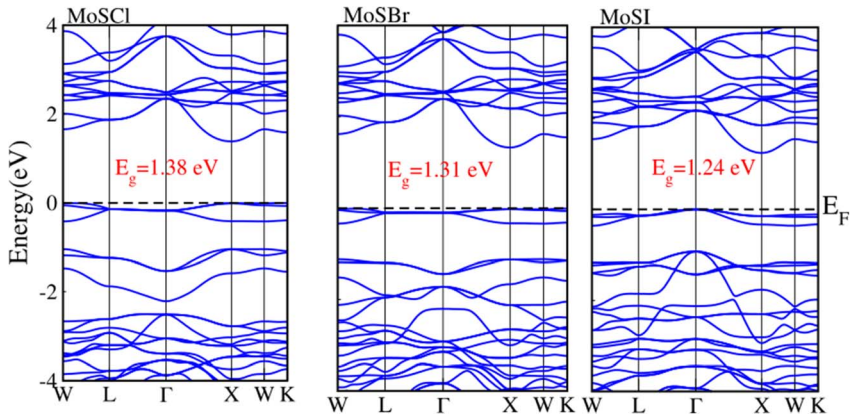


Fig. 2 Electronic band structure of MoSX (X = Br, Cl, I).

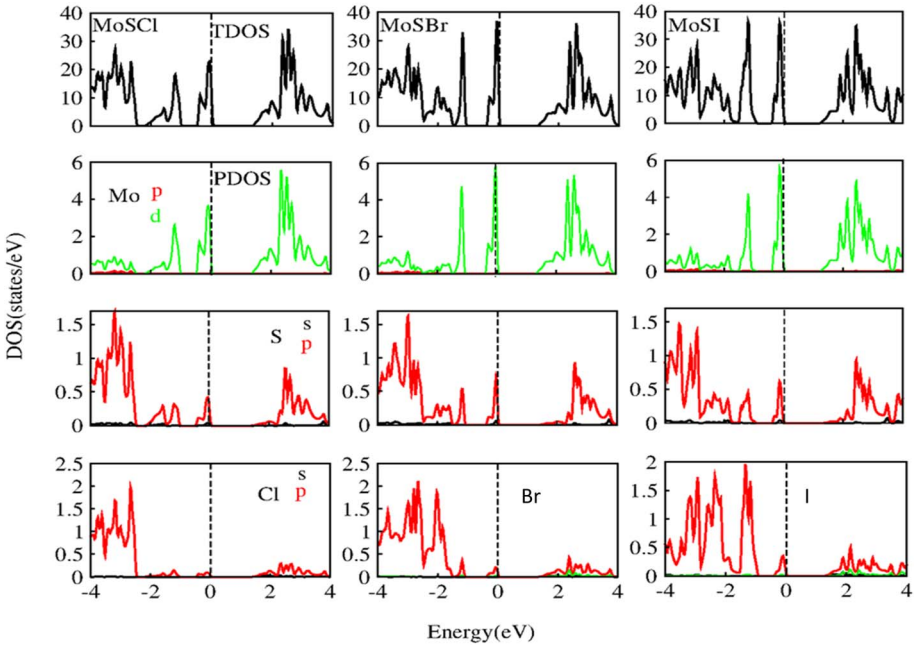


Fig. 3 The calculated DOS and contributions of orbitals of different atoms of MoSBr, MoSCl, and MoSI.

The stability of the MoSX (X = Cl, Br, I) is confirmed by the Debye temperature ($\theta_D$). From tensor matrix of Charpin,[41] the value of $\theta_D$ could be computed in terms of average sound velocity, as given in the relation below ;[42–44]

$$\theta_D = \left(\frac{h}{k_B}\right)\left(\frac{3n}{4\pi}\frac{N_A\rho}{M}\right)^{\frac{1}{3}} v_m$$

where $M$ is molar mass, $N_A$ is Avogadro number, $\rho$ is density, and average sound velocity is presented by $v_m$.

From the transverse parts of the Navior equations $v_t$ and the longitudinal $v_l$, the average sound velocity can be found out by the following relation:

$$v_m = \left(\frac{1}{3}\left(\frac{2}{v_t^3}+\frac{1}{v_l^3}\right)\right)^{-\frac{1}{3}}$$

here longitudinal ($v_l$) and transverse velocities ($v_t$) as have separately been expressed as under:

$$v_t = \left(\frac{G}{\rho}\right)^{\frac{1}{2}}$$

$$v_l = \left(\frac{(3B + 4G)}{\rho}\right)^{\frac{1}{2}}$$

The computed value of has been expressed in Table 2. The calculated $s$ $\theta_D$ and sound velocities provide valuable information on the lattice dynamics and thermal transport properties of MoSX (X = Cl, Br, I). The $\theta_D$ is directly related to the highest vibrational frequency of the lattice and reflects the stiffness of the crystal. A higher $\theta_D$ indicates stronger interatomic bonding and lower lattice anharmonicity, which are favorable for enhanced thermal conductivity. Among the studied compounds, MoSI exhibits the highest $\theta_D$ (642.4 K), indicating stronger bonding and a stiffer lattice, whereas MoSCl shows the lowest $\theta_D$ (453.9 K), suggesting relatively softer lattice vibrations compared to MoSBr and MoSI. This trend correlates with the increase in atomic mass from Cl to I, leading to enhanced phonon frequencies and thus higher $\theta_D$ in the iodide compound.

The calculated Debye temperatures and acoustic sound velocities are summarized in Table 2. These parameters provide important insight into the lattice dynamics and thermal transport behavior of the MoSX (X = Cl, Br, I) double perovskites. The Debye temperature ($\theta_D$) reflects the lattice stiffness and strength of interatomic bonding.

Similarly, the longitudinal ($v_l$) and transverse ($v_t$) sound velocities, along with the average sound velocity ($v_m$), increase in the order MoSCl < MoSBr < MoSI, which again confirms the higher lattice rigidity of MoSI. The higher sound velocities in MoSI imply faster phonon transport and potentially higher lattice thermal conductivity, while MoSCl is expected to show comparatively lower phonon transport efficiency due to its lower sound velocity values.

These observations are also consistent with the bandgap trend (MoSCl = 1.38 eV > MoSBr = 1.31 eV > MoSI = 1.24 eV). The compound with the largest bandgap (MoSCl) shows weaker lattice stiffness, while the one with the smallest bandgap (MoSI) exhibits stronger bonding and more compact lattice dynamics. Overall, the results highlight how the halide substitution significantly influences lattice vibration behavior and thermal transport properties, which is crucial in evaluating their suitability for thermal management and optoelectronic applications.

Table 2 The calculated Debye temperature ($\theta_D$), longitudinal ($v_l$) and transverse velocities ($v_t$), and average sound velocity ($v_m$) of MoSCl, MoSBr and MoSI

| | $m_e$ | $m_h$ | $\theta_D$ (K) | $v_t$ (m s$^{-1}$) | $v_l$ (m s$^{-1}$) | $v$m (m s$^{-1}$) | Ref. |
|---|---|---|---|---|---|---|---|
| MoSCl | 0.29 | 0.75 | 453.9 | 5838.4 | 9754.6 | 5460.2 | 43 and 44 |
| MoSBr | 0.23 | 0.94 | 470.7 | 6232.9 | 10 186.8 | 6881.6 | 43 and 44 |
| MoSI | 0.19 | 1.04 | 642.4 | 8828.0 | 14 722.3 | 9766.5 | 43 and 44 |

### 3.4 Optical charecteristics

The complex dielectric function $\varepsilon(\omega)$, corresponding to the incident photon energy ($E = \hbar\omega$), is expressed as:$\varepsilon(\omega) = \varepsilon_1(\omega) + i\varepsilon_2(\omega)$, where $\varepsilon_1(\omega)$ and $\varepsilon_2(\omega)$ denote the real and imaginary parts, respectively. The real part, $\varepsilon_1(\omega)$, is plotted for MoSX (X = Cl, Br, I) in Fig. 4. This component reflects the polarizability of the studied MoSX (X = Cl, Br, I) within the incident energy range of 0–8 eV. The $\varepsilon_1(0)$ at zero frequency are computed to be 9.11, 9.13, and 10.0 for MoSCl, MoSBr and MoSI, respectively (seen in Fig. 4(a)). Notably, $\varepsilon_1(0)$ increases as the halogen anion varies from Cl to I. This trend correlates with a reduction in the band gap ($E_g$), as observed in the electronic properties, which are inversely related to each other and consistent with Penn's model.[45]

Beyond the zero-frequency limit, $\varepsilon_1(\omega)$ increases, reaching maximum values at energies of 2.12 eV, 2.15 eV, and 1.96 eV for MoSX (X = Cl, Br, I), respectively. After attaining these maxima, $\varepsilon_1(\omega)$ declines with increasing incident energy. The real dielectric function exhibits distinct peaks as a function of incident energy, arising from transitions between discrete energy levels in the valence and conduction bands.[7,11] Notably, $\varepsilon_1(\omega)$ becomes negative for all three double perovskites within the energy range 6.0–7.5 eV, indicating a metallic character in this regime. The imaginary part of the dielectric function, $\varepsilon_2(\omega)$, quantifies photon absorption within the 0–8.0 eV range. This absorption results from electronic excitations from occupied valence-band states to unoccupied conduction-band states, as illustrated in Fig. 4(b). The $\varepsilon_2(\omega)$ spectra for all three perovskites exhibit a linear increase beyond distinct absorption edges, which correspond to their respective electronic band gaps (see Fig. 4). The first prominent absorption peaks for MoSX (X = Cl, Br, I) occur at 3.51 eV, 2.98 eV, and 2.39 eV, respectively. A systematic red shift in these peaks is observed as the halogen anion varies from Cl to I, consistent with the trend in the calculated band gaps.

Additionally, the complex refractive index, $n(\omega)$, was computed for MoSX (X = Cl, Br, I), as shown in Fig. 4(c). Comparative analysis both the $\varepsilon_1(\omega)$ and $n(\omega)$ exhibit analogous energy-dependent behavior. We determined the $n(0)$ from the low-energy extrapolation, yields values of 3.01, 3.02, and 3.16 for MoSX (X = Cl, Br, I), respectively. These values satisfy the

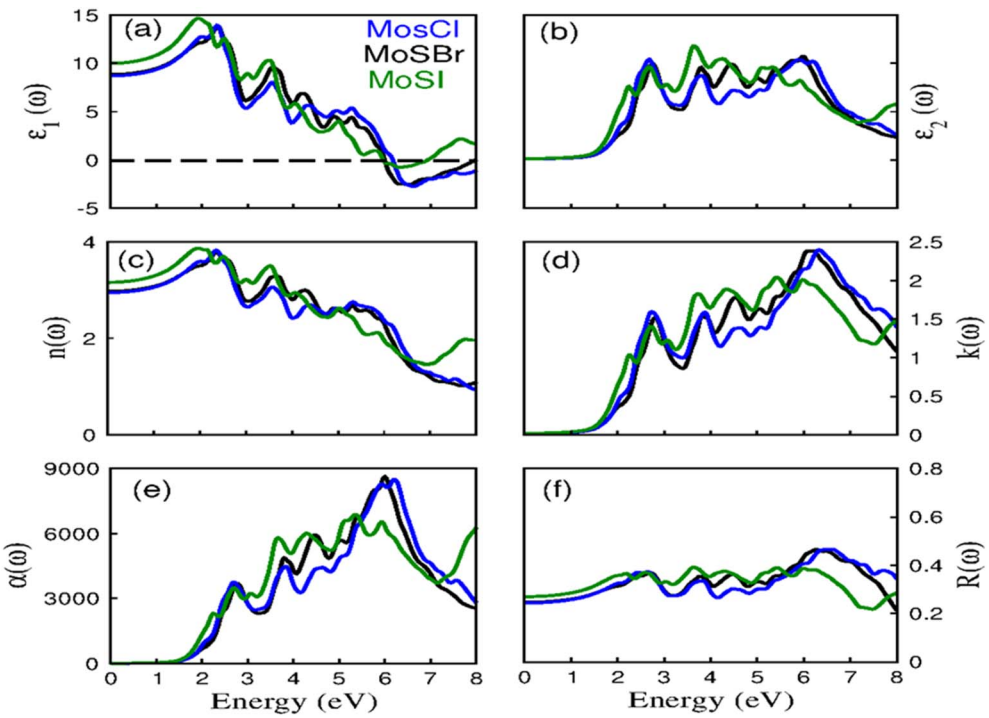


Fig. 4 The simulated optical characteristics in terms of (a) the real part, (b) the imaginary part, (c) the refractive index, (d) the extinction coefficient, (e) the absorption coefficient, and (f) the refractivity for MoSX.

 

fundamental relation $\varepsilon_1(0) = n^2(0)$,[46] validating the consistency between dielectric and optical responses. Beyond the static limit, $n(\omega)$ reaches maximum values of 3.83, 3.85, and 3.88 at energies of 2.12 eV, 2.15 eV, and 1.96 eV for the respective compounds, followed by a monotonic decrease with increasing energy. Notably, $n(\omega)$ falls below unity at in the higher energies for the Cl, Br, and I, respectively. In higher energy regime, the materials exhibit superluminal propagation characteristics,[47] permitting photon transmission without significant phase retardation. Fig. 4(d) presents the extinction coefficient $k(\omega)$, which mirrors the behavior of the imaginary dielectric function $\varepsilon_2(\omega)$, confirming its role in characterizing optical absorption. Prominent absorption peaks occur in the energies range 2–7 eV for the respective compounds, in excellent agreement with the $\varepsilon_2(\omega)$ spectra.

The absorption coefficient $\alpha(\omega)$ quantifies electronic transitions from the valence to conduction bands induced by incident photons. The overall absorption intensity increases with photon energy, reaching prominent peaks at in the given energies range (shown in Fig. 4(e). The tunable absorption edges (spanning ultraviolet to visible energies) coupled with strong UV absorption suggest promising applications of these double perovskites in optoelectronic devices.

The optical reflectivity $R(\omega)$, which quantifies surface interactions, is presented in Fig. 4(f). The reflectivity peaks at higher energies correlate with the onset of metallic behavior, as evidenced by negative values of the real dielectric function $\varepsilon_1(\omega)$. The tunable optical properties, particularly in the visible-to-UV range, suggest promising applications in optoelectronic devices and energy-harvesting technologies.

### 3.5 Thermoelectric characteristics

Optimizing thermoelectric performance requires materials with high efficiency to effectively convert waste heat into usable energy. The BoltzTrap code[48] was used to compute key thermoelectric and thermodynamic parameters. In this work, the temperature-dependent (200–800 K) behavior of the Seebeck coefficient ($S$), electrical conductivity ($\sigma/\tau$), electronic thermal conductivity ($K_e/\tau$), and power factor ($S^2\sigma/\tau$) are analyzed, as illustrated in Fig. 5. Superior thermoelectric materials exhibit a high power factor and figure of merit ($ZT$), necessitating a large Seebeck coefficient, high electrical conductivity, and minimal lattice thermal conductivity.[2,49,50]

The $\sigma/\tau$ arises from the movement of free charge carriers (electrons or holes) and exhibits a temperature-dependent increase due to enhanced carrier kinetic energy (Fig. 5(a)). The $\sigma/\tau$ increases with the increasing temperature. One can observed from the Fig. 5(a), that the $\sigma/\tau$ decreases when we go from Cl to I. This decrease may be due to the increasing molecular size, results in weaker overlap between their p-orbitals, leading to less efficient electron delocalization.

The Seebeck coefficient ($S$), a key parameter reflecting the thermoelectric voltage induced by a thermal gradient, demonstrates high sensitivity to temperature (Fig. 5 (b)). At 100 K, the $S$ values for at 200 K for MoSCl (180 μV K$^{-1}$), MoSBr (148 μV K$^{-1}$), and MoSI (224 μV K$^{-1}$) decreases to 130 μV K$^{-1}$, 125 μV K$^{-1}$, and 150 μV K$^{-1}$ at 800 K. The sustained high Seebeck coefficients suggest strong thermoelectric response even at elevated temperatures. The Seebeck coefficient ($S$) varies with the anion substitution (Cl → Br → I), correlating with the reduction in

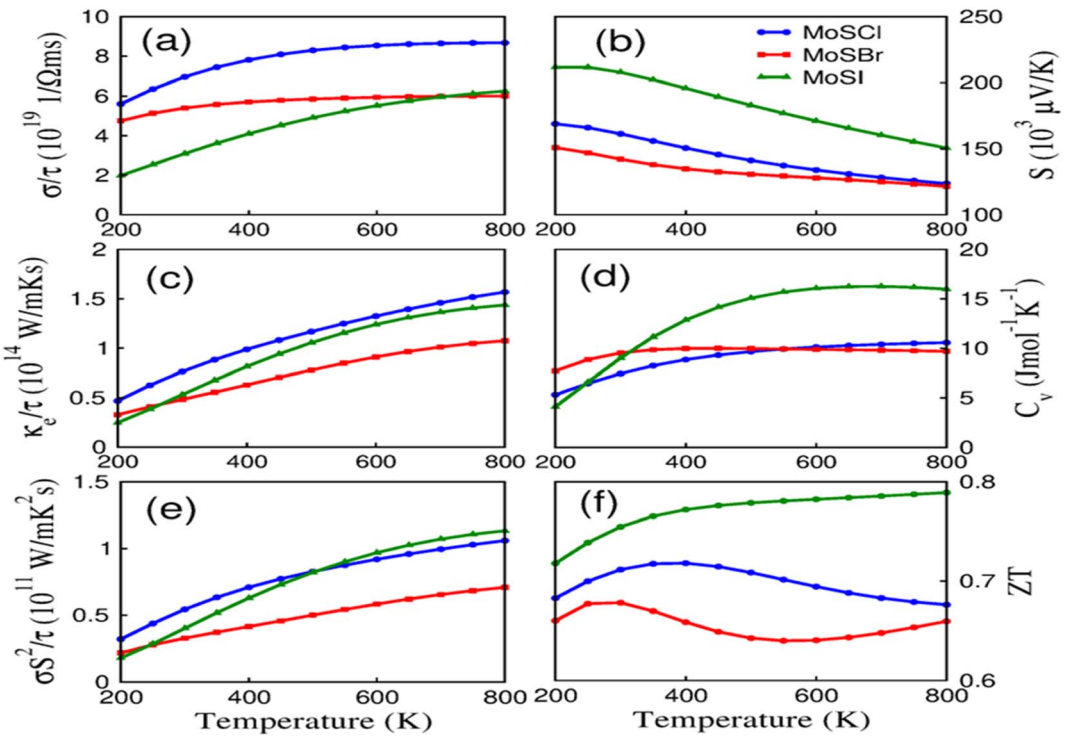


Fig. 5 The calculated theromoelectric properties in terms of (a) electrical conductivity, (b) seebeck coefficient, (c) thermal conductivity, (d) heat-capacity, (e) power-factor, and (f) figure of merit for MoSX (X = Cl, Br, I).

band gap ($E_g$). As the band gap narrows from Cl to I, the charge carrier density increases, requiring less energy for carrier excitation, thereby enhancing electrical conductivity.

Thermal conductivity in these materials is dominated by electronic contributions ($K_e/\tau$), as phonon effects are negligible. As depicted in Fig. 5(c), $K_e/\tau$ increase from 0.23–031 W K$^{-1}$ m$^{-1}$ s$^{-1}$ (200 K) to 0.54–1.05 W K$^{-1}$ m$^{-1}$ s$^{-1}$(800 K) for MoSX (X= Cl, Br, I). The low thermal conductivity is desirable for efficient thermoelectric performance.

Additionally, we have calculated the heat capacity ($C_v$), representing the thermal energy storage capacity, rises with temperature (Fig. 5(d)). The MoSCl, and the MoSBr take the lead to reach the Dulong-petit asymptotes at $T \sim 400$ K and the MoSI reaches to asymptotes value with relatively higher temperature ($T \sim 600$ K). Moreover, the $C_v$ increase from 4.4–7.8 J mol$^{-1}$ K$^{-1}$ (200 K) to 9.95–16.5 J mol$^{-1}$ K$^{-1}$ (800 K) for MoSX (X= Cl, Br, I). This trend indicates superior thermal stability for $Cs_2InBiI_6$, suggesting its potential for high-temperature thermoelectric applications.

The power factor (PF $= S^2\sigma/\tau$), a critical metric for device applications, is derived from the Seebeck coefficient and electrical conductivity. Fig. 5(e) and 6(a) illustrates a significant enhancement in PF across the temperature range: MoSCl (0.33–1.1 $\times$ 10$^{11}$ W K$^{-2}$ m$^{-1}$ s$^{-1}$), MoSBr (0.19–0.58 $\times$ 10$^{11}$ W K$^{-2}$ m$^{-1}$ s$^{-1}$), and MoSI (0.186–1.37 $\times$ 10$^{11}$ W K$^{-2}$ m$^{-1}$ s$^{-1}$). This trend underscores the potential of the MoSX (X = Cl, Br, I) for high-temperature thermoelectric applications, provided phase stability is maintained. Notably, the PF exhibits higher magnitudes on the p-type region due to the enhanced $S$ in this regime. The figure of merit ($ZT$) is a decisive metric for evaluating the efficiency of thermoelectric materials in thermal energy conversion devices.[49,50]

The dependence of $ZT$ on chemical potential ($\mu$) illustrated in Fig. 5(f) and 6(b). At optimal carrier concentration the $ZT$ values approach unity for n-/p-type regimes. At 300 K, the $ZT$ values for MoSCl, MoSBr, and MoSI are computed to be 0.69, 0.62, and 0.76, respectively, demonstrating their potential for thermoelectric applications. Our calculated values of $ZT$ at 300 K are higher than the available experimental study on ReSTe (0.4).[51] Thus, the investigated MoSX (X = Cl, Br, I) compounds exhibit promising thermoelectric performance, making them viable candidates for energy conversion applications.

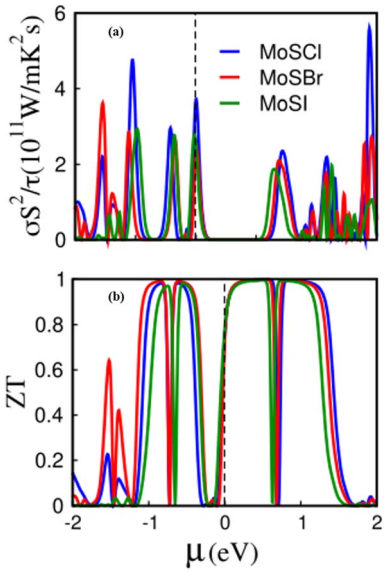


Fig. 6 The calculated (a) power-factor, and (b) figure of merit with restive chemical potential for MoSX (X = Cl, Br, I).

# 4 Conclusion

In this work we have investigated the optoelectronics and thermoelectric properties of MoSX (X = Cl, Br, I) using the first-principles calculations. It has been predicted that all the configurations exhibit energetically favorable nature with lower formation energies. The MoSX (X = Cl, Br, I) shows a semiconductor nature. Interestingly, the MoSCl and MoSBr possesses a direct band gap, which could be promising for the applications in LEDs, and optical devices. Additionally, the optical results depicted that the MoSX (X = Cl, Br, I) can efficiently absorb light in the visble and UV region. Furthermore, the $ZT$ values shows the suitable nature of MoSX (X = Cl, Br, I) for the thermal device. Thus, based on our findings suggest a fundamental framework for the experimentalist for suitable applications in solar power generator and thermal energy management.

## Author contributions

Muhammad Yousaf: performed the calculations and wrote the original draft. Ali Raza: performed the calculations and wrote the original draft. Farooq Ali: formal analysis, edit and review the final draft. Hamid Ullah: supervision, edit and review the final draft. Young-Han Shin: computational facility. Essam A. Al-Ammar: calculations and revised the manuscript.

## Conflicts of interest

The authors declare that they have no known competing financial interests or personal relationships that could have appeared to influence the work reported in this paper.

## Data availability

Data used in this research work will be made available on request from the authors.

## Acknowledgements

This work was funded by the Ongoing Research Funding program (ORF-2025-492), King Saud University, Riyadh, Saudi Arabia.

## References

1 K. F. Mak, C. Lee, J. Hone, J. Shan and T. F. Heinz, Atomically Thin MoS2: A New Direct-Gap Semiconductor, *Phys. Rev. Lett.*, 2010, **105**(13), 136805.

2 A. Wahab, F. Ali, M. Asghar, H. Ullah, S. Iftikhar, Y.-H. Shin, R. Sharma and E. A. Al-Ammar, Exploration of Sn-Based Janus Materials for Emerging Renewable Energy Applications, *Phys. B Condens. Matter*, 2025, **698**, 416755, DOI: 10.1016/j.physb.2024.416755.

3 H. S. Waheed, H. Ullah, M. Waqas Iqbal and Y.-H. Shin, Optoelectronic and Photocatalytic Properties of Mo-Based Janus Monolayers for Solar Cell Applications, *Optik*, 2022, 170071, DOI: 10.1016/j.ijleo.2022.170071.

4 H. S. Waheed, H. Ullah, Y.-H. Shin and Y. M. Alanazi, Enhanced Device Absorption Efficiency and Photocatalytic Response of Monolayer PtX2 (X = S, Se, Te) for Photocatalysis and Solar Cell Applications, *Phys. Status Solidi B*, 2023, **260**(7), 2300028, DOI: 10.1002/pssb.202300028.

5 A. O. M. Almayyali, B. B. Kadhim and H. R. Jappor, Stacking Impact on the Optical and Electronic Properties of Two-Dimensional MoSe2/PtS2 Heterostructures Formed by PtS2 and MoSe2 Monolayers, *Chem. Phys.*, 2020, **532**, 110679, DOI: 10.1016/j.chemphys.2020.110679.

6 *Valley-dependent spin polarization in bulk MoS2 with broken inversion symmetry - PubMed*, https://pubmed.ncbi.nlm.nih.gov/25064393/, accessed 2022-06-10.

7 H. S. Waheed, M. Asghar, H. S. Ahmad, T. Abbas, H. Ullah, R. Ali, M. J. I. Khan, M. W. Iqbal, Y.-H. Shin, M. S. Khan and R. Neffati, Janus MoSO and MoSSe Monolayers: A Promising Material for Solar Cells and Photocatalytic Applications, *Phys. Status Solidi B*, 2022, **260**, 2200267, DOI: 10.1002/pssb.202200267.

8 Th. Böker, R. Severin, A. Müller, C. Janowitz, R. Manzke, D. Voß, P. Krüger, A. Mazur and J. Pollmann, Band Structure of ${\mathrm{MoS}}_{2},$ ${\mathrm{MoSe}}_{2},$ and $\ensuremath{\alpha}\ensuremath{-}{\mathrm{MoTe}}_{2}:$ Angle-Resolved Photoelectron Spectroscopy and Ab Initio Calculations, *Phys. Rev. B:Condens. Matter Mater. Phys.*, 2001, **64**(23), 235305, DOI: 10.1103/PhysRevB.64.235305.

9 Y. Zhou, W. Liu, X. Huang, A. Zhang, Y. Zhang and Z. L. Wang, Theoretical Study on Two-Dimensional MoS2 Piezoelectric Nanogenerators, *Nano Res.*, 2016, **9**(3), 800–807, DOI: 10.1007/s12274-015-0959-8.

10 F. Li, W. Wei, H. Wang, B. Huang, Y. Dai and T. Jacob, Intrinsic Electric Field-Induced Properties in Janus MoSSe van Der Waals Structures, *J. Phys. Chem. Lett.*, 2019, **10**(3), 559–565, DOI: 10.1021/acs.jpclett.8b03463.

11 M. Alam, H. S. Waheed, H. Ullah, M. W. Iqbal, Y.-H. Shin, M. J. Iqbal Khan, H. I. Elsaeedy and R. Neffati, Optoelectronics Properties of Janus SnSSe Monolayer for Solar Cells Applications, *Phys. B Condens. Matter*, 2022, **625**, 413487, DOI: 10.1016/j.physb.2021.413487.

12 R. Chaurasiya and A. Dixit, Defect Engineered MoSSe Janus Monolayer as a Promising Two Dimensional Material for NO2 and NO Gas Sensing, *Appl. Surf. Sci.*, 2019, **490**, 204–219.

13 A.-Y. Lu, H. Zhu, J. Xiao, C.-P. Chuu, Y. Han, M.-H. Chiu, C.-C. Cheng, C.-W. Yang, K.-H. Wei, Y. Yang, Y. Wang, D. Sokaras, D. Nordlund, P. Yang, D. A. Muller, M.-Y. Chou, X. Zhang and L.-J. Li, Janus Monolayers of Transition Metal Dichalcogenides, *Nat. Nanotechnol.*, 2017, **12**(8), 744–749, DOI: 10.1038/nnano.2017.100.

14 Y.-C. Lin, D. O. Dumcenco, Y.-S. Huang and K. Suenaga, Atomic Mechanism of the Semiconducting-to-Metallic Phase Transition in Single-Layered MoS2, *Nat. Nanotechnol.*, 2014, **9**(5), 391–396, DOI: 10.1038/nnano.2014.64.

15 S.-D. Guo, X.-S. Guo, R.-Y. Han and Y. Deng, Predicted Janus SnSSe Monolayer: A Comprehensive First-Principles Study, *Phys. Chem. Chem. Phys.*, 2019, **21**(44), 24620–24628, DOI: 10.1039/C9CP04590B.

16 M. Asghar, H. Ullah, M. W. Iqbal, Y.-H. Shin and R. Neffati, Defects Mediated Electronic and Magnetic Properties of Monolayer Janus SnSSe, *Mater. Today Commun.*, 2023, **35**, 106124, DOI: 10.1016/j.mtcomm.2023.106124.

17 S.-D. Guo, X.-S. Guo, R.-Y. Han and Y. Deng, Predicted Janus SnSSe Monolayer: A Comprehensive First-Principles Study, *Phys. Chem. Chem. Phys.*, 2019, **21**(44), 24620–24628, DOI: 10.1039/C9CP04590B.

18 H. Alam and S. Ramakrishna, A Review on the Enhancement of Figure of Merit from Bulk to Nano-Thermoelectric Materials, *Nano Energy*, 2013, **2**(2), 190–212, DOI: 10.1016/j.nanoen.2012.10.005.

19 M. A. Fox and M. T. Dulay, *Heterogeneous Photocatalysis*, ACS Publications, DOI: 10.1021/cr00017a016.

20 M. Kibbou, Z. Haman, I. Essaoudi and A. Ainane, Designing New Halide Double Perovskite Materials Rb2AgGaX6 (X: Br, Cl) with Direct Band Gaps and High Power Conversion Efficiency, *J. Solid State Chem.*, 2023, **317**, 123698, DOI: 10.1016/j.jssc.2022.123698.

21 M. Hussain, F. Ali, H. Ullah, A. Ali, Y.-H. Shin and K. M. Elhindi, Strain Dependent Physical Properties of the Lead-Free Perovoskite ZnZrO3 for Energy Device Applications, *Solid State Commun.*, 2025, **397**, 115846, DOI: 10.1016/j.ssc.2025.115846.

22 Strain Modulated Physical Properties of Double Perovskite Rb2InGaCl6 for the Possible Energy Applications, *Phys. B Condens. Matter* 2025, **701**, 416975, DOI: 10.1016/j.physb.2025.416975.

23 Y. Li, J. Wang, B. Zhou, F. Wang, Y. Miao, J. Wei, B. Zhang and K. Zhang, Tunable Interlayer Coupling and Schottky Barrier in Graphene and Janus MoSSe Heterostructures by Applying an External Field, *Phys. Chem. Chem. Phys.*, 2018, **20**(37), 24109–24116, DOI: 10.1039/c8cp04337j.

24 P. Blaha, K. Schwarz, F. Tran, R. Laskowski, G. Madsen and L. Marks, WIEN2k: An APW+lo Program for Calculating the Properties of Solids, *J. Chem. Phys.*, 2020, **152**, 074101, DOI: 10.1063/1.5143061.

25 G. K. H. Madsen, Functional Form of the Generalized Gradient Approximation for Exchange: The PBE $\alpha$ Functional, *Phys. Rev. B: Condens. Matter Mater. Phys.*, 2007, **75**(19), 195108, DOI: 10.1103/PhysRevB.75.195108.

26 T. Katsura and Y. A. Tange, Simple Derivation of the Birch–Murnaghan Equations of State (EOSs) and Comparison with EOSs Derived from Other Definitions of Finite Strain, *Minerals*, 2019, **9**(12), 745, DOI: 10.3390/min9120745.

27 Z. Bordjiba, A. Meddour and C. Bourouis, Ab Initio Theoretical Prediction of Structural, Electronic, and Magnetic Properties in the 3d (Mn)-Doped Zinc-Blende MgSe: A DFT-mBJ Approach, *J. Supercond. Novel Magn.*, 2018, **31**(7), 2261–2270, DOI: 10.1007/s10948-017-4495-5.

28 N. A. Noor, M. W. Iqbal, T. Zelai, A. Mahmood, H. M. Shaikh, S. M. Ramay and W. Al-Masry, Analysis of Direct Band Gap A2ScInI6 (A=Rb, Cs) Double Perovskite Halides Using DFT Approach for Renewable Energy Devices, *J. Mater. Res. Technol.*, 2021, **13**, 2491–2500, DOI: 10.1016/j.jmrt.2021.05.080.

29 F. Aslam, H. Ullah and M. Hassan, Theoretical Investigation of Cs2InBiX6 (X = Cl, Br, I) Double Perovskite Halides Using First-Principle Calculations, *Mater. Sci. Eng., B*, 2021, **274**, 115456, DOI: 10.1016/j.mseb.2021.115456.

30 P. Hohenberg and W. Kohn, Inhomogeneous Electron Gas, *Phys. Rev.*, 1964, **136**(3B), B864–B871, DOI: 10.1103/PhysRev.136.B864.

31 A. Jain, S. P. Ong, G. Hautier, W. Chen, W. D. Richards, S. Dacek, S. Cholia, D. Gunter, D. Skinner, G. Ceder and K. A. Persson, Commentary: The Materials Project: A Materials Genome Approach to Accelerating Materials Innovation, *APL Mater.*, 2013, **1**, 4812323, DOI: 10.1063/1.4812323.

32 F. Aslam, H. Ullah and M. Hassan, First Principle Study of Band Gap Tuning in Cs2InSbX6 (X= Cl, Br, I) for Optoelectronic and Thermoelectric Applications, *Phys. Scr.*, 2022, **97**(4), 045801.

33 Magneto-Optic and Photocatalytic Response of CuCrX3 (X=Cl, Br, I) for Energy Storage Applications, *Comput. Condens. Matter*, 2025, **42**, e00997, DOI: 10.1016/j.cocom.2024.e00997.

34 F. Aslam, B. Sabir and M. Hassan, Structural, Electronic, Optical, Thermoelectric, and Transport Properties of Indium-Based Double Perovskite Halides Cs2InAgX6 (X = Cl, Br, I) for Energy Applications, *Appl. Phys. A*, 2021, **127**(2), 112, DOI: 10.1007/s00339-020-04178-x.

35 H. Ullah, M. Noor-A-Alam, H. J. Kim and Y.-H. Shin, Influences of Vacancy and Doping on Electronic and Magnetic Properties of Monolayer SnS, *J. Appl. Phys.*, 2018, **124**(6), 065102, DOI: 10.1063/1.5022151.

36 H. Ullah, M. Noor-A-Alam and Y.-H. Shin, Vacancy- and Doping-Dependent Electronic and Magnetic Properties of Monolayer SnS2, *J. Am. Ceram. Soc.*, 2020, **103**(1), 391–402, DOI: 10.1111/jace.16739.

37 K. Choudhary, Q. Zhang, A. C. E. Reid, S. Chowdhury, N. Van Nguyen, Z. Trautt, M. W. Newrock, F. Y. Congo and F. Tavazza, Computational Screening of High-Performance Optoelectronic Materials Using OptB88vdW and TB-mBJ Formalisms, *Sci. Data*, 2018, **5**(1), 180082, DOI: 10.1038/sdata.2018.82.

38 D. Koller, F. Tran and P. Blaha, Merits and Limits of the Modified Becke-Johnson Exchange Potential, *Phys. Rev. B: Condens. Matter Mater. Phys.*, 2011, **83**(19), 195134, DOI: 10.1103/PhysRevB.83.195134.

39 T. Nakajima and K. Sawada, Discovery of Pb-Free Perovskite Solar Cells via High-Throughput Simulation on the K Computer, *J. Phys. Chem. Lett.*, 2017, **8**(19), 4826–4831, DOI: 10.1021/acs.jpclett.7b02203.

40 X.-G. Zhao, J.-H. Yang, Y. Fu, D. Yang, Q. Xu, L. Yu, S.-H. Wei and L. Zhang, *Design of Lead-Free Inorganic Halide Perovskites for Solar Cells via Cation-Transmutation*, ACS Publications, DOI: 10.1021/jacs.6b09645.

41 T. Charpin, A Package for Calculating Elastic Tensors of Cubic Phase Using WIEN, *Laboratory of Geometrix*, Paris, 2001.

42 M. Bilal, Saifullah, M. Shafiq, B. Khan, H. A. Rahnamaye Aliabad, S. Jalali Asadabadi, R. Ahmad and I. Ahmad, Antiperovskite Compounds SbNSr3 and BiNSr3: Potential Candidates for Thermoelectric Renewable Energy Generators, *Phys. Lett. A*, 2015, **379**(3), 206–210, DOI: 10.1016/j.physleta.2014.11.016.

43 N. A. Noor, M. Rashid, G. M. Mustafa, M. I. Khan, A. Mahmood and S. M. Ramay, Study of Pressure Induced Physical Properties of ZnZrO3 Perovskite Using Density Functional Theory, *Chem. Phys. Lett.*, 2020, **753**, 137601.

44 F. Ali, M. Hussain, H. Ullah, J.-T. Wang and M. Alomar, Optoelectronic and Thermoelectric Response of Lead-Free Halide Double Perovskites $Rb_2$ $BiAuX_6$ (X = Cl, Br, I) for Energy Storage Applications, *RSC Adv.*, 2025, **15**(45), 37999–38013, DOI: 10.1039/D5RA04508H.

45 D. R. Penn, Wave-Number-Dependent Dielectric Function of Semiconductors, *Phys. Rev.*, 1962, **128**(5), 2093–2097, DOI: 10.1103/PhysRev.128.2093.

46 M. Fox, Optical Properties of Solids, *Am. J. Phys.*, 2002, **70**(12), 1269–1270, DOI: 10.1119/1.1691372.

47 D. Mugnai, A. Ranfagni and R. Ruggeri, Observation of Superluminal Behaviors in Wave Propagation, *Phys. Rev. Lett.*, 2000, **84**(21), 4830.

48 G. K. H. Madsen and D. J. Singh, BoltzTraP. A Code for Calculating Band-Structure Dependent Quantities, *Comput. Phys. Commun.*, 2006, **175**(1), 67–71, DOI: 10.1016/j.cpc.2006.03.007.

49 F. Ali, M. Asghar, H. S. Waheed, H. Ullah, M. J. I. Khan, G. Anwar, M. Amin, S. M. Wabaidur and Y.-H. Shin, Optoelectronic and Thermoelectric Response of Lead Free Halide Double Perovskites Rb2AgPX6 (X = Cl, Br, I) for Energy Storage Applications, *Opt. Quant. Electron.*, 2024, **56**(7), 1094, DOI: 10.1007/s11082-024-07005-2.

50 M. Asghar, H. S. Waheed, U. Abbas, H. Ullah, M. J. I. Khan, S. M. Wabaidur, A. Ali and Y.-H. Shin, A Computational Approach to Study the Halides-Based Double Perovskites Cs2InAuX6 (X=Cl, Br) for Low-Cost Energy Technologies, *Phys. Rev. B*, 2024, **682**, 415916, DOI: 10.1016/j.physb.2024.415916.

51 H. Matsumoto, H. Isomura, K. Kojima, R. Okuma, H. Ohshima, C.-H. Lee, Y. Yamakawa and Y. Okamoto, Cubic ReSTe as a High-Performance Thermoelectric Material, *Appl. Phys. Lett.*, 2025, **126**, 243903, DOI: 10.1063/5.0268567.